JACS
JOURNAL OF THE AMERICAN CHEMICAL SOCIETY
pubs.acs.org/JACS
Article

Colossal Room-Temperature Magnetoelectric Coupling in Anion-Deficient Layered Perovskite Films with Ordered Cation Distribution

Hongwei Wang,[▽] Xiangfei Li,[▽] Jun Miao,*[,▽] Kun Lin, Qiang Li, Xin Chen, Yili Cao, Xi Shen, Youwen Long, Yu Chen, Jiaou Wang, Jing Zhou, Yi Wang, Qiliang Li, Richeng Yu,* and Xianran Xing*

Cite This: J. Am. Chem. Soc. 2025, 147, 24382−24391
Read Online

ACCESS | Metrics & More | Article Recommendations | Supporting Information

ABSTRACT: The anion-deficient layered perovskite $Pb_2Fe_2O_5$, featuring a polarizable active Pb cation with lone pair electrons and a magnetically active transition metal Fe cation, presents a promising candidate for multiferroic applications. Nonetheless, the exploration of multiferroic properties and magnetoelectric coupling in $Pb_2Fe_2O_5$ is extremely rare due to its complex structure. Herein, a colossal magnetoelectric coupling coefficient (5.19×10^5 mV cm^{-1} Oe^{-1}), high ferroelectric polarization (2 μC/cm^2), and magnetic moment (25 emu/cc) at room temperature have been discovered in an epitaxial $Pb_{2+0.48}Fe_2O_5$ film. The findings of this study demonstrate that the introduction of excessive Pb ions can disrupt the disordered arrangement of the mixed layer and convert it to an ordered distribution to improve ferroelectric properties. This research not only enriches the magnetoelectric coupling material system but also offers a viable strategy for achieving strong room-temperature magnetoelectric coupling and multiferroicity in layered oxide materials.

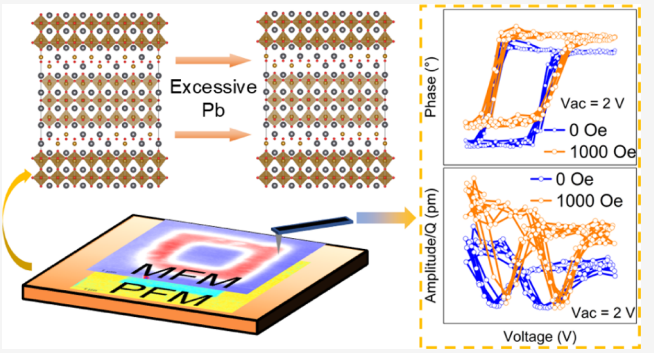

INTRODUCTION

Single-phase multiferroic films with magnetoelectric (ME) coupling are promising in information storage, such as electric write-in and magnetic read-out, which can significantly improve storage speed and reduce energy consumption.[1−4] However, the conflict in electronic structures for ferroelectricity (necessitating empty d orbitals) and ferromagnetism (requiring partially filled d orbitals) typically renders the incompatibility for these two characteristics.[5] Therefore, developing single-phase multiferroic films at room temperature is challenging.[6] Compared to single-phase multiferroics, composite materials show a larger ME coupling coefficient for their flexible design strategies, such as materials selection (e.g., strong piezoelectric and magnetostrictive materials), composite architecture designs (0−0 nanodot, 0−3 and 1−3 architectures), etc.[7−9] Nonetheless, the inherent high magnetic moments and coercive fields of strong magnetostrictive components generate stray magnetic fields, limiting their compatibility with ME logic device requirements.[10] Additionally, the complexity of these architectures elevates fabrication costs and technical challenges.[11] Therefore, it is still necessary to explore room-temperature single-phase multiferroic materials with high ME coupling coefficients to meet the application requirements. Conversely, single-phase multiferroics face intrinsic limitations in compositional diversity and tunability, constraining ME coupling enhancements and practical scalability. This challenge necessitates the exploration of novel material systems through crystallographic engineering to reconcile these mutually exclusive properties.

Layered oxides including Ruddlesden−Popper ($A_2A'_{n-1}B_nO_{3n+1}$) and Aurivillius ($(Bi_2O_2)(A_{n-1}B_nO_{3n+1})$) phases exhibit additional atomic planes compared to simple perovskites. These structures can be engineered through strain engineering, perovskite layers' regulation, and abundant chemical doping to active emergent functionalities, such as ferroelectricity,[12,13] ferromagnetism,[14] multiferroicity,[15−19] and polar vortex.[20] Hence, layered oxides due to their multiple adjustable dimensions, compared to perovskite-based oxides, provide a promising material platform for achieving room-temperature multiferroicity and correlated ME coupling. However, there is still a limited number of studies on the ME coupling effect of layered oxide films, and their ME coupling coefficients are much lower than those of $BiFeO_3$ and conventional composite films.[4,17,18,21−23] Fortunately, they have at least pioneered a way to go in the field.

Another layered oxide (i.e., anion-deficient layered oxide) appears to have been overlooked in the realm of multiferroics,

Received: February 10, 2025
Revised: June 24, 2025
Accepted: June 25, 2025
Published: July 2, 2025

https://doi.org/10.1021/jacs.5c01840
J. Am. Chem. Soc. 2025, 147, 24382−24391

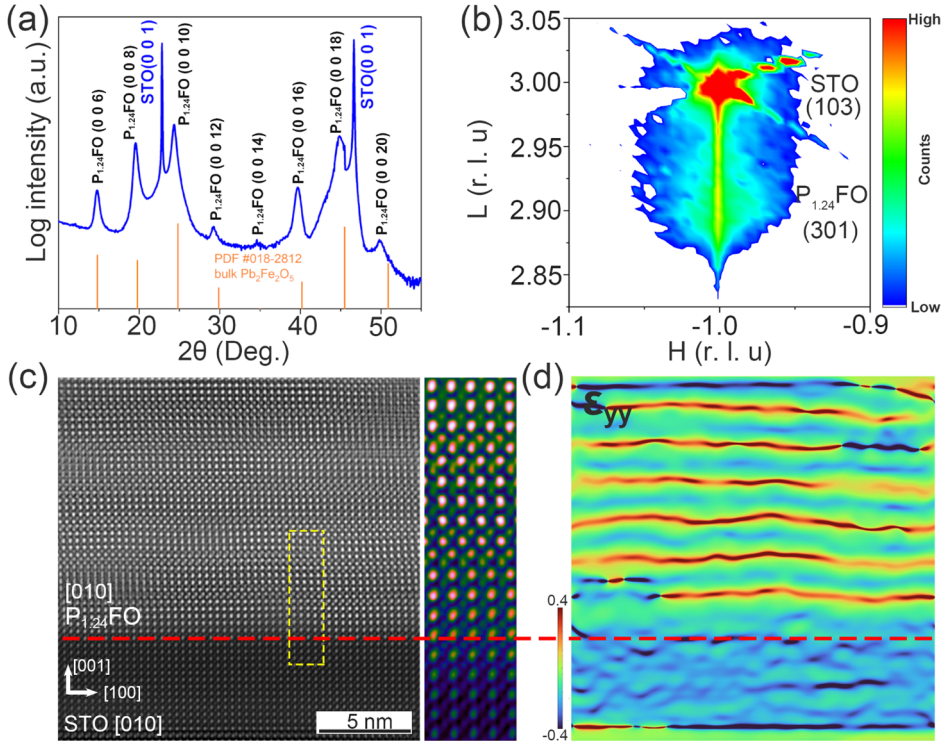

Figure 1. Structure characterization of $P_{1.24}FO$ films. (a) Synchrotron-based out-of-plane $\theta/2\theta$ XRD pattern. (b) RSM near the (103) spot of the STO substrate. (c) HAADF image around $P_{1.24}FO$−STO interface along the STO [010] zone axis. (d) The out-of-plane strain ε_{yy} image of (c) by the geometric phase analysis (GPA).

likely due to its intricate structure. To date, only $Pb_2Fe_2O_5$ bulk ceramics[24] and multiphase films with PbO and Fe_2O_3 impurities[25] have been reported to exhibit room-temperature ferroelectricity and magnetism. Unlike conventional layered oxides, the additional atomic planes of anion-deficient perovskite $Pb_2Fe_2O_5$ are formed by crystallographic shear into quasi-two-dimensional planes composed of both Pb and Fe ions bonding with O^{2-} ions, meaning that the metal ion sites are co-occupied by Pb and Fe ions, known as mixed layers,[26] as shown in Figure S2a. The disordered distribution of Pb and Fe ions in mixed layers leads to a centrosymmetric structure (space group $I4/mmm$). However, the weak ferroelectricity has been observed in $Pb_2Fe_2O_5$ bulk ceramics.[24] This indicates that the $Pb_2Fe_2O_5$ bulk should contain structurally polar components potentially related to the distribution of Pb and Fe ions in mixed layers. In other words, the disordered distribution of Pb/Fe ions indicates that the energy of Pb and Fe ions occupying the same lattice points in the mixed layers is proximity. Local disturbances may disrupt the disordered distribution and lead to the formation of polarization structures in local structures, resulting in weak ferroelectricity. Hence, altering the stoichiometric ratio is anticipated to regulate the distribution of Pb and Fe in the mixed layer, consequently impacting the ferroelectric and magnetic characteristics.

In this work, the enhanced multiferroicity and strong ME coupling of single-phase $Pb_{2+0.48}Fe_2O_5$ ($P_{1.24}FO$) films are induced by the reordered distribution of Pb/Fe cations in mixed layers. The high ME coupling coefficient (5.19×10^5 mV cm^{-1} Oe^{-1}) at room temperature of single-phase $P_{1.24}FO$ films reaches the same level as that of conventional piezoelectric/piezomagnetic composite films. For the $P_{1.24}FO$ and $Pb_{2+0.1}Fe_2O_5$($P_{1.05}FO$) films with different stoichiometric ratios, the former exhibits stronger ME coupling and a ferroelectric response. Scanning transmission electron microscopy (STEM), synchrotron X-ray absorption spectroscopy (XAS), and density functional theory (DFT) calculations prove that the locally ordered distribution of Pb/Fe ions in mixed layers is responsible for the high ferroelectric polarization ($P_r \sim 2\ \mu C/cm^2$) in $P_{1.24}FO$ films. The mixed layers of single-phase $P_{1.24}FO$ films play a crucial role in enhancing multiferroic properties and the strong ME coupling coefficient. This research not only enriches the magnetoelectric coupling material system (i.e., anion-deficient layered perovskite oxide) but also indicates that regulating the additional atomic planes of layered materials is an effective method for achieving strong room-temperature magnetoelectric coupling and multiferroicity.

RESULTS AND DISCUSSION

The epitaxial $P_{1.24}FO$ films were grown on (001)-orientated $SrTiO_3$ (STO) substrates by radio frequency magnetron sputtering. The out-of-plane synchrotron X-ray diffraction (SXRD) pattern of the $P_{1.24}FO$ film with (00l) orientation is shown in Figure 1a. The characteristic peak positions of $P_{1.24}FO$ films shifted toward a low angle relative to the bulk $Pb_2Fe_2O_5$ ($a = b = 3.9047$ Å, $c = 36$ Å) due to excessive Pb ions increasing crystal cell parameters c. Reciprocal space mapping (RSM) around STO (103) evidenced that the $P_{1.24}FO$ film was coherently strained to the STO substrate, as shown in Figure 1b. The average in-plane and out-of-plane lattice parameters of the $P_{1.24}FO$ film were estimated by RSM, as shown in Figure S1 and Table S1. The low-magnification high-angle annular dark-field (HAADF) image (Figure S2b) showed the obvious interface between the $P_{1.24}FO$ film and STO substrate in a large range. The $P_{1.24}FO$ film thickness was

https://doi.org/10.1021/jacs.5c01840
J. Am. Chem. Soc. 2025, 147, 24382−24391

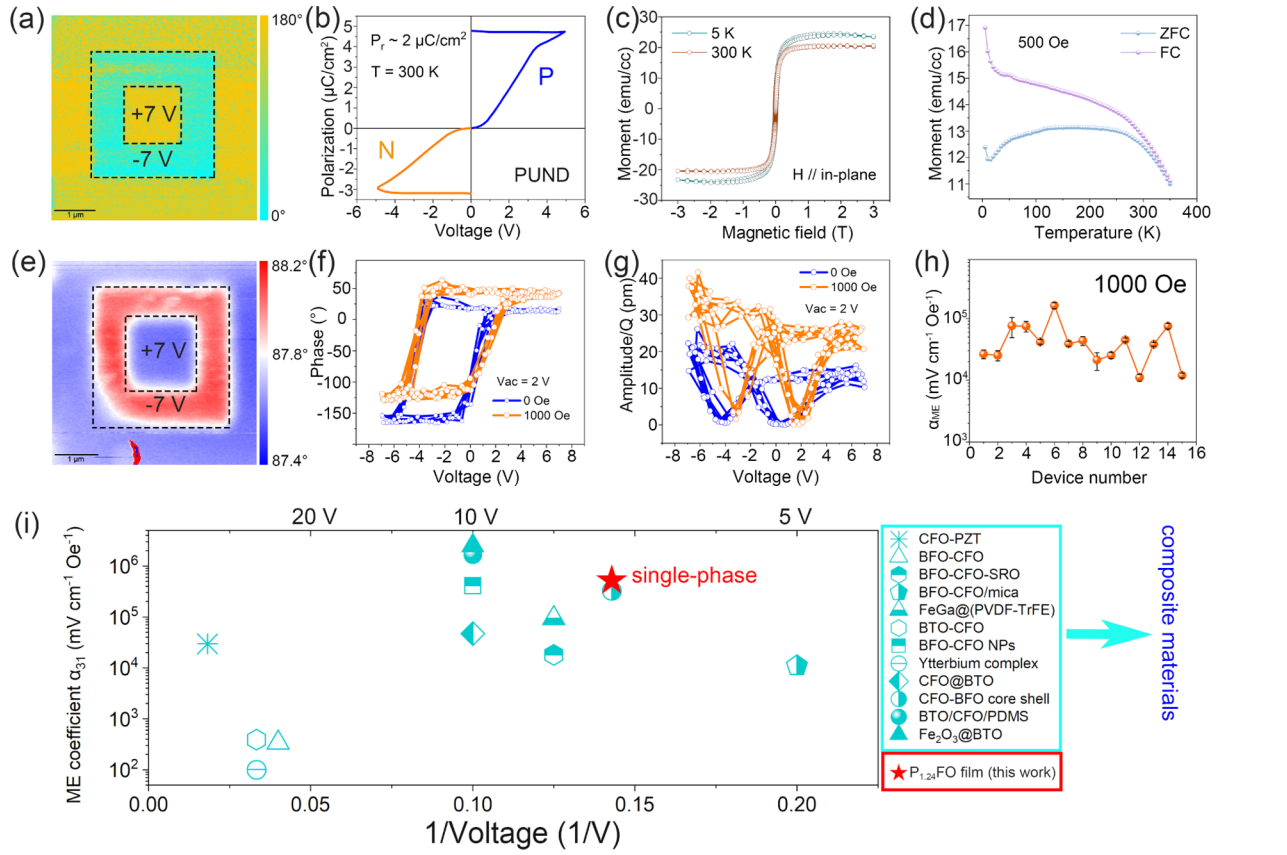

Figure 2. Multiferroicity and magnetoelectric coupling of $P_{1.24}FO$ films. (a) Out-of-plane ferroelectric domain image after writing box-in-box image with +7 V/−7 V. (b) The *P*−*V* loops obtained by PUND measurement. (c) The magnetic hysteresis loops of $P_{1.24}FO$ films at 5 and 300 K, where the magnetic field is parallel to the in-plane. (d) Temperature-dependent magnetic moment curves (ZFC and FC) at a magnetic field of 500 Oe. (e) Out-of-plane magnetic domain image after writing box-in-box image with +7 V/−7 V. (f,h) The piezoelectric response characteristics of $P_{1.24}FO$ films, including phase−voltage hysteresis loops (f) and amplitude−voltage butterfly loops (g) with and without the application of an external magnetic field of 1000 Oe. (h) ME coupling coefficient at different regions in $P_{1.24}FO$ films. (i) Comparison of the microscopic ME coefficient α_{31} and operating voltage of $P_{1.24}FO$ films with those of previously reported materials measured by PFM. Abbreviation: CFO ($CoFe_2O_4$), PZT ($Pb(Zr_{0.52}Ti_{0.48})O_3$), BFO ($BiFeO_3$), SRO ($SrRuO_3$), and BTO ($BaTiO_3$).

approximately 46 nm at a growth time of 60 min, in agreement with the fitting results from X-ray reflectivity (XRR, Figure S2c). The selected area electron diffraction (SAED, Figure S2d) pattern indicated that the $P_{1.24}FO$ film possessed good single crystallinity. The HAADF image (Figure 1c) along the [010] zone axis demonstrated that the $P_{1.24}FO$ film was composed of perovskite layers and mixed layers and was arranged layer by layer along the out-of-plane direction (the structural diagram is shown in Figure S2a). The ε_{yy} strain mapping (Figures 1d and S3a,b) of the $P_{1.24}FO$ film exhibited a horizontal striped distribution along the [001] direction due to the difference of out-of-plane lattice parameters between the perovskite layers and mixed layers, which is a characteristic of layered structure.[27] In addition, with the increasing film thickness, the continuity of stripes was disrupted (Figure S3b) due to many dislocations (Figure S4a,b) being generated to release stress induced by excessive Pb ions.

The ferroelectric properties of $P_{1.24}FO$ films were demonstrated through piezoresponse force microscopy (PFM) and positive-up-negative-down (PUND) methods. In Figure 2a, the box-in-box pattern was written by applying a voltage of +7 V/−7 V to the probe at a 5 × 5 μm^2 region of $P_{1.24}FO$ films using the PFM mode. The PFM phase contrast changed from orange to cyan with a 180° domain switching. The macroscopic polarization of the Pt/$P_{1.24}FO$/$SrRuO_3$(SRO, 13 nm) capacitor was measured by the PUND method which can eliminate nonswitching contributions,[28−30] where amplitude and width of voltage triangle were 5 V and 0.5 ms, respectively (Figure S5a). The impact of the SRO buffer layer on the structure of the $P_{1.24}FO$ film has been detailed in the Supporting Information. It should be noted that the displacement current confirmed the ferroelectric characteristics of $P_{1.24}FO$ films.[31] Figure 2b shows the polarization−voltage (*P*−*V*) loops calculated by the PUND measurement, where the calculation method is presented in Supporting Information. The true P_r value of the $P_{1.24}FO$ film was about 2 $\mu C\ cm^{-2}$ on average ($P_r = \frac{P_{+max}/2 + P_{-max}/2}{2}$), which is 1 order of magnitude higher than the $Pb_2Fe_2O_5$ bulk.[24] Notably, the remnant polarization of positive voltage was higher than that of negative voltage, which indicated the presence of a built-in electric field in the $P_{1.24}FO$ film. The built-in electric field can be attributed to the asymmetric distribution of oxygen vacancies ($V_O^{\bullet\bullet}$) and the flexoelectric field. The existence of oxygen vacancies was confirmed by X-ray photoelectron spectroscopy (XPS, Figure S5d) and electron energy loss spectroscopy (EELS, Figure S6). The oxygen vacancies were mainly distributed near the surface and easily accumulated in defect areas (e.g., dislocations, as shown in the Figures S4 and S5c), forming a built-in electric field point from the Pt top

https://doi.org/10.1021/jacs.5c01840
J. Am. Chem. Soc. 2025, 147, 24382−24391

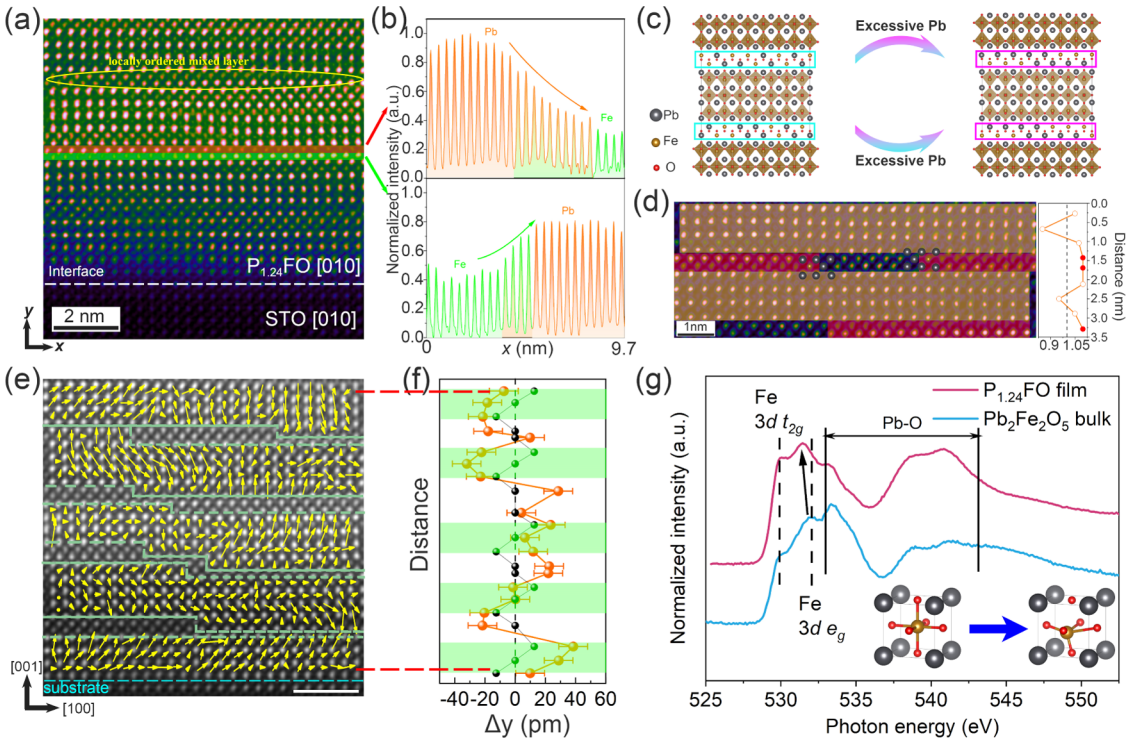

Figure 3. Origin of ferroelectric and magnetic enhancement. (a) Atomically resolved HAADF image of the $P_{1.24}FO$ film viewed along the STO [010] zone axis. (b) The intensity of atom columns' intensity profile of the red region and the green region (a) along the *x* direction. (c) The schematic diagram: introducing excessive Pb leads to a locally ordered distribution of Pb/Fe ions in mixed layers. (d) HAADF image of mixed layers in the $P_{1.24}FO$ film. The orange box areas represent perovskite layers. The red box areas represent additional perovskite unit cells due to locally ordered atomic distribution. Right image: the average *c*/*a* of each perovskite unit cell layer along the thickness direction. (e) Polarization distribution map of perovskite blocks, superimposed to STEM-HAADF image along the [010] zone axis, where scale bar represents 2 nm. (f) Fe cations displacement of the $P_{1.24}FO$ film (orange ball) and simulated $Pb_2Fe_2O_5$ bulk (black ball) projected along the [001] zone axis. (g) O-*K* edge XAS spectra of the $P_{1.24}FO$ film and $Pb_2Fe_2O_5$ bulk.

electrode to SRO bottom electrode.[32] The positive in-plane strain gradient along film thickness (Figure S3c,d) could also lead to a built-in electric field from Pt to SRO. The detailed discussion on the built-in electric field can be found in the Supporting Information. The asymmetric leakage current−voltage curve (Figure S5e) also indicated the presence of a built-in electric field in $P_{1.24}FO$ films.[33] If the applied voltage (negative voltage) was opposite the built-in electric field, a larger voltage was required to polarize to the same polarization state as the positive voltage. Therefore, the remnant polarization (P_r) value of the negative voltage part was lower than that of the positive voltage part. Figure 2c shows the magnetic hysteresis loops of the $P_{1.24}FO$ film at 5 and 300 K. The $P_{1.24}FO$ films showed weak ferromagnetic characteristics with a low coercive field (~70 Oe), which is beneficial for achieving low-voltage controlled magnetization reversal and reducing power consumption.[34,35] In addition, the remnant magnetization (M_r) of $P_{1.24}FO$ films was 2.357 emu/cc (0.286 emu/g) at room temperature, which was higher than bulk $Pb_2Fe_2O_5$ (0.037 emu/g).[24] The field cooling (FC) curve and zero-field cooling (ZFC) curve indicated that the magnetic ordering temperature (Néel temperature, T_N) was higher than 350 K (Figure 2d). To understand the effect of oxygen vacancies on magnetism, we measured the magnetic hysteresis of $P_{1.24}FO$ films at room temperature before and after air annealing (400 °C, 1 h) in a muffle furnace, as shown in Figure S5f. The saturation magnetic moment (M_s) of $P_{1.24}FO$ film decreased from 25 to 5 emu/cc after annealing, which indicated that oxygen vacancies can enhance the magnetism of $P_{1.24}FO$ film. In a word, in the case of excessive Pb, the epitaxial $P_{1.24}FO$ film possessed the coexistence of stronger ferroelectricity and magnetism than $Pb_2Fe_2O_5$ bulk at room temperature.

The ME coupling response at room temperature is more important than independent ferroelectricity and magnetism for single-phase multiferroic materials. The scanning probe microscopy (SPM) technique could characterize the local ME coupling behavior of the film.[7−9,36] In Figure 2e, the box-in-box patterns were written by applying a voltage of +7 V/−7 V at other 5 × 5 μm^2 regions of $P_{1.24}FO$ films using the PFM mode, then reading magnetic domains using the magnetic force microscopy (MFM) mode. The magnetic domains also exhibited box-in-box patterns (Figure 2e), which indicated that applying voltage can regulate the magnetic domain switching of the $P_{1.24}FO$ film. To further measure the ME effect, the lateral ME coefficient α_{31} could be estimated from the variation in piezoelectric amplitude butterfly loops induced by a lateral magnetic field,[37] as shown in Figure 2f,g. The α_{31} can be described as the ratio of the longitudinal electric field ΔE_3 to the lateral magnetic field ΔH_1:[37]

$$\alpha_{31} = \frac{\Delta E_3}{\Delta H_1} = \frac{\Delta \mu/(d_{33}\cdot D)}{\Delta H_1} \quad (1)$$

where μ is the piezoresponse amplitude (amplitude/quality factor Q) in dual frequency resonant tracking piezoresponse measurement, $d_{33} = \mu/V$ under zero magnetic field, and V is the alternating current (AC) voltage, and D is the thickness of $P_{1.24}FO$ film. In this work, $\Delta\mu$ = 15.39 pm Q^{-1} and μ = 12.9

https://doi.org/10.1021/jacs.5c01840
J. Am. Chem. Soc. 2025, 147, 24382−24391

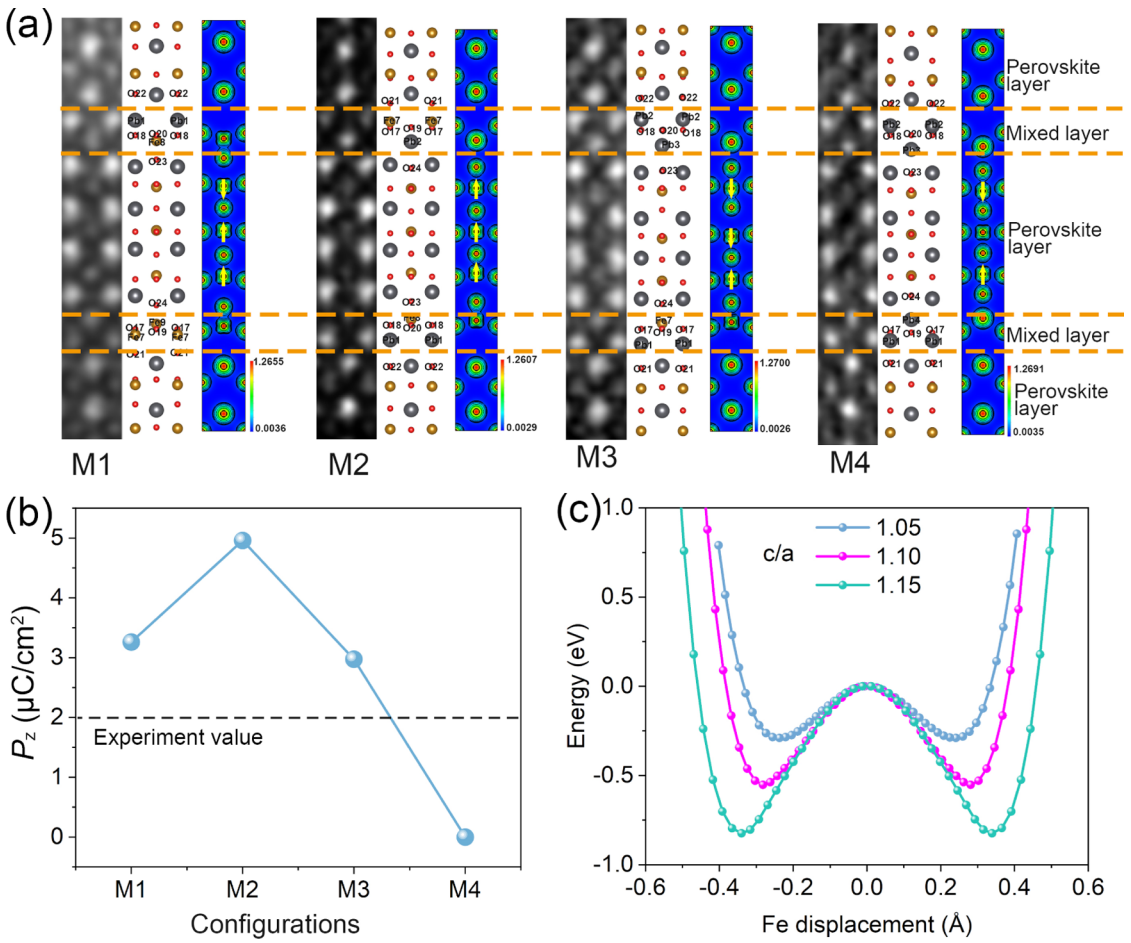

Figure 4. DFT calculation of ferroelectric origin and enhancement. (a) HAADF images correspond to M1, M2, M3, and M4 configurations in the $P_{1.24}FO$ film, and their charge density distribution. The yellow arrow represents the direction of the dipole moment of the perovskite unit cell. (b) Theoretical calculation values of out-of-plane polarization for M1, M2, M3, and M4. (c) Ferroelectric double-well energy landscape of perovskite unit cells with different c/a ratios.

pm Q^{-1} could be obtained according to the butterfly loops (Figure 2g) at zero direct current (DC) bias voltage, D = 46 nm, V = 2 V, and ΔH_1 = 1000 Oe. Therefore, the lateral ME coupling coefficient α_{31} = 5.19 × 10^5 mV cm^{-1} Oe^{-1} was obtained. To demonstrate the universality of ME coupling in $P_{1.24}FO$ films, we measured the ME coupling coefficient in different regions, as shown in Figure 2h, showing that the ME coupling coefficient of the $P_{1.24}FO$ film ranges from 10^4 mV cm^{-1} Oe^{-1} to 10^5 mV cm^{-1} Oe^{-1}. Moreover, we sequentially measured the amplitude butterfly loops under magnetic fields of 0 Oe, 1000 Oe, −1000 Oe, and returning to 0 Oe, as shown in Figure S7a. After applying a magnetic field, the maximum piezoelectric amplitude increased, and once the magnetic field was removed, the piezoelectric amplitude reverted to a level close to its original state (Figure S7b), indicating that the ME coupling behavior of the $P_{1.24}FO$ film is reversible and reproducible. Figure S7c shows the estimated ME coupling coefficients under varying magnitudes of positive and negative magnetic fields. This observation aligned with the existing literature[38,39] that the ME coupling coefficients decrease with increasing magnetic field when it exceeds the magnetic coercive field. In general, the ME coefficient of single-phase multiferroic materials was much lower than that of composite multiferroic materials.[40] Figure 2i shows the ME coupling coefficient of $P_{1.24}FO$ films and other materials with the same measurement method as this work.[7−9,36,37,41−47] Excitingly, single-phase $P_{1.24}FO$ films exhibited significant ME coupling coefficients at low operating voltage, offering benefits such as simplified manufacturing compared to composite films. These characteristics support the potential industrial utilization of low-power ME memory. In the Supporting Information, we briefly discussed the influence of different Pb/Fe ratios on ME coupling, ferroelectric response, and magnetism.

The origin of enhanced ferroelectric polarization in the $P_{1.24}FO$ film was also discussed. Interestingly, we observed the ordered distribution of Pb/Fe atomic columns in mixed layers of the $P_{1.24}FO$ film by STEM (Figure 3a). The red area and green area showed a gradual transition from Pb atomic columns (high contrast) to Fe atomic columns (low contrast) and Fe atomic columns to Pb atomic columns along the x direction, respectively. To gain a clearer understanding of the atomic distribution of mixed layers, the strength distribution of the atomic columns along the x direction is shown in Figure 3b. The strength transition of atomic columns from high to low indicated an elemental transition from Pb atomic columns to Fe atomic columns, and vice versa. It should be noted that the structure cannot be interpreted as an out-of-plane boundary (OPB) of Aurivillius oxides.[20,48] First, the $Pb_2Fe_2O_5$ bulk structure differed from Aurivillius oxides on the additional atomic planes (Figure S8a). If Pb ions occupy Fe_3 lattice sites, Aurivillius oxides can be formed, but this situation does not exist in $P_{1.24}FO$ films according to STEM. Second, if it is

https://doi.org/10.1021/jacs.5c01840
J. Am. Chem. Soc. 2025, 147, 24382−24391

believed that stacking faults lead to OPB, based on the $Pb_2Fe_2O_5$ bulk structure, the adjacent atomic layers of the mixed layers should show low contrast in the HAADF image (Figure S8b, green box) but that has high contrast in experimental observation (Figure 3a). So, the ordered distribution of Pb/Fe atomic columns should be caused by the introduction of excessive Pb atoms to disrupt the stoichiometric ratio, as shown in Figure 3c. As shown in Figure 3d, the locally ordered atomic distribution in the mixed layer of $P_{1.24}FO$ films led to the formation of additional perovskite unit cells (red region) with large c/a.

The ferroelectricity of layered materials such as Aurivillius oxides originates from the displacement of central ions in the perovskite layers.[49,50] Therefore, the additional perovskite unit cells increased the ferroelectric component in the $P_{1.24}FO$ films, which may be the reason for the enhancement of ferroelectricity. Figure 3e shows the polarization distribution of perovskite blocks in the $P_{1.24}FO$ film along the [010] zone axis. According to the Born effective charge calculation (see Methods), the polarization magnitude mainly ranges from 0.53 to 4.24 $\mu C\ cm^{-2}$, aligning with experimental evidence (Figure 2b), suggesting that the ferroelectric polarization in $P_{1.24}FO$ films stemmed from the perovskite blocks. In Aurivillius ferroelectric oxides, the mirror symmetric polarization along the [001] direction leads to a zero net out-of-plane polarization.[20,49,50] Nevertheless, the out-of-plane polarization orientations within a single unit cell of the $P_{1.24}FO$ films were uniform, leading to an overall out-of-plane polarization. To better demonstrate the polarization distribution of $P_{1.24}FO$ films, the average displacement of Fe cations in each perovskite layer along the [001] direction was statistically analyzed, as shown in Figure 3e. It can be clearly seen that the Fe cations in the perovskite layers within a $P_{1.24}FO$ unit cell had the same direction of ion shifts (Figure 3f, green region), which also proved that the $P_{1.24}FO$ unit cells had nonzero out-of-plane polarization, indicating that locally ordered distribution of Pb/Fe ions was conducive to the out-of-plane polarization. In addition, the Pb_{Fe} antisite defects (Figure S9) were beneficial for enhancing out-of-plane polarization, despite their influence on the surrounding 2 nm region. The discussion on antisite defects is presented in the Supporting Information.

Figure 3g shows O K-edge XAS spectra of the $P_{1.24}FO$ film and $Pb_2Fe_2O_5$ bulk, where two lower peaks are attributed to the hybridization between O 2p and Fe 3d t_{2g} and e_g orbitals, respectively. Compared with the FeO_6 octahedron with a splitting energy of 2.1 eV in $Pb_2Fe_2O_5$ bulk, the splitting energy of $P_{1.24}FO$ film reduced to 1.6 eV. Moreover, t_{2g} orbital energy remained unchanged and e_g orbital energy shifted toward low energy, which also indicated that Fe ions deviated from the octahedral center.[31,51] The ratio of t_{2g} to e_g in the $P_{1.24}FO$ film was greater than that in the $Pb_2Fe_2O_5$ bulk, indicating a decrease in the occupation of t_{2g} orbitals and an increase in the occupation of e_g orbitals in the $P_{1.24}FO$ films. This promoted the formation of high spin states and increased the magnetic moment of Fe,[52] thereby enhancing magnetism.

The locally ordered distribution of Pb/Fe ions in mixed layers led to the universal existence of four competitive structures in the $P_{1.24}FO$ film, as observed through STEM (Figures 4a and S10a,b). First, the total energies of Pb occupying different positions (mixed layers and perovskite layers) were calculated using the S0 structure as a reference phase. (The calculation models are shown in Figure S10c). In Table S2, we compared the energies of Pb ions occupying different positions, which indicated that excessive Pb ions are more likely to occupy the mixed layers than the perovskite layers. However, these results do not represent that excessive Pb ions all occupy the mixed layer in actual $P_{1.24}FO$ film; they may also reside in the perovskite layer, forming antisite defects (Figure S9), a common occurrence in Pb-based perovskite oxides.[53,54] To elucidate the impact of Pb occupying the mixed layer on the perovskite layer, we computed the charge densities of the M1, M2, M3, and M4 configurations. As shown in Figure 4a, excessive Pb asymmetrically occupying the mixed layer (M1, M2, M3) disrupted the mirror displacement (not net displacement) of Fe ions in perovskite layers, leading to a nonzero net displacement. Due to the central symmetry of the M4 configuration, only M1, M2 and M3 configurations contributed to ferroelectric polarization in the $P_{1.24}FO$ film.

The out-of-plane polarization (P_z) values of different structures were calculated via the Born effective charge method. As shown in Figure 4b, the M4 configuration exhibits central inversion symmetry and has no net out-of-plane polarization. In contrast, the polar structures (M1, M2, and M3) are generated when Pb atoms partially occupy the mixed layers. It is noteworthy that while the $P_{1.24}FO$ film contained a coexistence of M1, M2, M3, and M4 configurations, only the first three contributed to ferroelectric polarization. Therefore, it is reasonable for the experimental polarization value to be lower than the theoretically calculated one. Additionally, Table S3 shows space groups of the four configurations, the number of perovskite cells, and their Fe ions displacement. The partial substitution of Pb ions within the mixed layers induced the formation of a polar structure ($P4mm$), enhancing the polarity component (number of perovskite units) and the net displacement of Fe ions, in agreement with experimental observations (Figure 3d,e). To understand the polarization contribution of the c/a ratio of perovskite unit cells in the $P_{1.24}FO$ film, the Landau energy landscapes of perovskite unit cells with varying c/a ratios in the M2 structure were calculated, as shown in Figure 4c. With the movement of Fe atoms, the total energy of these systems featured a classic ferroelectric double-well potential.[55] The increase of the c/a ratio led to larger displacement of Fe ions, indicating that perovskite unit cells with a large c/a ratio facilitated enhanced polarization.

CONCLUSION

A novel material, an anion-deficient layered perovskite oxide $P_{1.24}FO$ film, was explored for multiferroic ME coupling. The mixed layers could be easily controlled to achieve emergent performance. The high ME coupling coefficient and ferroelectric polarization at room temperature were achieved in $Pb_{1.24}FO$ films with an ordered Pb/Fe ions distribution in the mixed layers. The ordered Pb/Fe ions distribution within mixed layers disrupted the central symmetry, resulting in nonzero out-of-plane displacement of Fe ions within PFO unit cells. This structural distortion increased the polarity component and c/a axis ratio of perovskite cells, which in turn enhanced room-temperature ferroelectric polarization. This approach that regulates the atomic arrangement within additional atomic planes presents a potential pathway for layered oxides to exhibit multiferroic properties and robust ME coupling at room temperature.

https://doi.org/10.1021/jacs.5c01840
J. Am. Chem. Soc. 2025, 147, 24382−24391

METHODS

Growth of $P_{1.24}FO$ and $P_{1.05}FO$ Films. $P_{1.24}FO$ and $P_{1.05}FO$ films were successively fabricated by radio frequency magnetron sputtering on $SrTiO_3(001)$ substrates using a single target with a nominal Pb/Fe ratio of 3:2. The preparation condition of a single target has been shown in the Supporting Information. Before depositing, the sputtering chamber was pumped to a high vacuum of 6×10^{-4} Pa, and then, the substrate was heated to 700 °C. The working pressure was 1 Pa with a pure argon environment. The power of the RF voltage source was 100 W. As the thickness increased, the Pb/Fe ratio also increased. For the $P_{1.24}FO$ film, the deposition time was 60 min, and for the $P_{1.05}FO$ film, the deposition time was 30 min. To measure the ferroelectricity of $P_{1.24}FO$ films, we first deposited the $SrRuO_3$ (13 nm) film as the bottom electrode on the $SrTiO_3$ substrate by direct-current (DC) magnetron sputtering, where the growth temperature was 750 °C, the pressure was 1.5 Pa (pure argon environment), and the power of DC voltage source was 30 W. The Pt top electrodes were deposited by DC magnetron sputtering at room temperature, where the pressure was 0.8 Pa, and the power of DC voltage source was 40 W.

X-ray Measurements. XRD and RSM data were obtained at the 1W1A Diffuse X-ray Scattering Station of the Beijing Synchrotron Radiation Facility (BSRF-1W1A) and Rigaku SmartLab X-ray diffractometer. The X-ray absorption spectroscopy (XAS) measurements were measured using the photoelectron spectroscopy station (4B9B beamline) of the Beijing Synchrotron Radiation Facility. X-ray photoelectron spectroscopy (XPS, Thermo Escalab 250Xi) was used to characterize the chemical valence and oxygen vacancies of the $P_{1.24}FO$ film.

Multiferroic and Magnetoelectric Coupling Measurements. To measure the ferroelectricity of the $P_{1.24}FO$ film, the Pt top electrodes and SRO bottom electrodes were deposited by magnetron sputtering at room temperature and 750 °C, respectively. Pt/$P_{1.24}FO$/SRO planar capacitors were measured using a ferroelectric tester (AiXACCT, TF analyzer 2000). PFM and MFM signals were measured using a commercial AFM system (Asylum Research MFP-3D, USA). The PFM and MFM images were collected by the TiIr-coated tip and the CoPt/FePt-coated magnetic tip, respectively. Magnetic data of the $P_{1.24}FO$ films were measured by using a magnetic property measurement system (MPMS-3, Quantum Design). The frequency response of the $P_{1.24}FO$ film was measured by an Agilent 4294A.

EDS and TEM Characterization. The Pb/Fe element ratios were determined by an Energy Dispersive Spectrometer (EDS, ULTIM MAX40) and scanning electron microscopy (SEM, Zeiss EVO18). High-quality thin cross-sectional samples for TEM were prepared by using the focused ion beam (FIB, Helios 600i, FEI) technique. The HAADF images and the SAED patterns were obtained on a JEOL ARM200F transmission electron microscope equipped with a double spherical aberration corrector at 200 kV. The HAADF images were collected at acceptance angles of 90−370 mrad.

Theory Calculations. Density functional theory (DFT) calculations were performed via the Vienna ab initio package by using projected augmented wave potential with a cutoff energy of 520 eV.[56−58] The Perdew−Burke−Ernzerhof (PBE) functional was employed in a generalized gradient approximation (GGA) for the exchange−correlation term.[59,60] We applied a Hubbard U (U = 4 eV) correction on d orbital of Fe.[61] Our GGA-PBE pseudopotentials included 4 valence electrons for Pb ($6s^26p^2$), 8 for Fe ($3d^74s^1$), and 6 for O ($2s^22p^4$). Brillouin-zone integrations were performed with a Gaussian smearing of 0.05 eV during all structural optimizations. For charge density and theoretical polarization calculations, the calculation models are shown in Figure S10c. The reciprocal space was sampled by gamma point in the Brillouin zone with a grid of 6 × 6 × 1. Geometry optimization was performed with a convergence condition of 1×10^{-5} eV per atom for the energy difference and a maximum force of 0.02 eV/Å. The theoretical ferroelectric polarization of the $P_{1.24}FO$ film was calculated by using the Born effective charge method:[62]

$$\delta P_i = \frac{e}{\Omega} \sum_{\alpha,j} Z_{ij}^{\alpha *} \delta_j^{\alpha}$$

where α represents the ion; i, j = x, y, z direction; δ_j^{α} is the displacement of the ion α in the j direction with respect to a reference phase; $Z_{ij}^{\alpha *}$ is the Born effective charge tensor for ion α; Ω is the volume of the cell; and e is the electron charge. The Born effective charges of Pb, Fe, and O ions were calculated by the density functional perturbation theory (DFPT) method (i.e., LEPSILON = .TRUE.),[63] where the Born effective charge of Fe ion was about 3.21 × 10^{-16} C.

For double-well energy landscape calculations, the $PbFeO_3$ perovskite unit cells with different c/a ratios were established according to optimized M1, M2, and M3 (Table S3). The reciprocal space was sampled by gamma point in the Brillouin zone with a grid of 6 × 6 × 6. Geometry optimization was performed with a convergence condition of 1×10^{-6} eV per atom for the energy difference and a maximum force of 0.01 eV/Å.

ASSOCIATED CONTENT

Data Availability Statement

All data needed to evaluate the conclusions in the paper are presented in the paper and/or the Supporting Information.

Supporting Information

The Supporting Information is available free of charge at https://pubs.acs.org/doi/10.1021/jacs.5c01840.

Process of PFO ceramic target, description of PUND method, analysis of the asymmetric polarization, influence of different Pb/Fe ratios on multiferroicity and ME coupling, description of antisite defect in the $P_{1.24}FO$ film, description of oxygen vacancies on ferroelectric switching, influence of the SRO buffer layer on the structure of the $P_{1.24}FO$ film, and additional DFT data (PDF)

AUTHOR INFORMATION

Corresponding Authors

Jun Miao − *Institute of Solid State Chemistry, University of Science and Technology Beijing, Beijing 100083, China; School of Materials Science and Engineering, University of Science and Technology Beijing, Beijing 100083, China;* orcid.org/0000-0002-6924-0737; Email: J.miao@ustb.edu.cn

Richeng Yu − *Beijing National Laboratory for Condensed Matter Physics, Institute of Physics, Chinese Academy of Sciences, Beijing 100190, China*; Email: rcyu@iphy.ac.cn

Xianran Xing − *Institute of Solid State Chemistry, University of Science and Technology Beijing, Beijing 100083, China;* orcid.org/0000-0003-0704-8886; Email: xing@ustb.edu.cn

Authors

Hongwei Wang − *Institute of Solid State Chemistry, University of Science and Technology Beijing, Beijing 100083, China; School of Materials Science and Engineering, University of Science and Technology Beijing, Beijing 100083, China;* orcid.org/0000-0002-8411-4827

Xiangfei Li − *Beijing National Laboratory for Condensed Matter Physics, Institute of Physics, Chinese Academy of Sciences, Beijing 100190, China*

Kun Lin − *Institute of Solid State Chemistry, University of Science and Technology Beijing, Beijing 100083, China;* orcid.org/0000-0003-4515-3206

Qiang Li − *Institute of Solid State Chemistry, University of Science and Technology Beijing, Beijing 100083, China;* orcid.org/0000-0003-4259-6984
Xin Chen − *Institute of Solid State Chemistry, University of Science and Technology Beijing, Beijing 100083, China*
Yili Cao − *Institute of Solid State Chemistry, University of Science and Technology Beijing, Beijing 100083, China;* orcid.org/0000-0003-0523-2073
Xi Shen − *Beijing National Laboratory for Condensed Matter Physics, Institute of Physics, Chinese Academy of Sciences, Beijing 100190, China*
Youwen Long − *Beijing National Laboratory for Condensed Matter Physics, Institute of Physics, Chinese Academy of Sciences, Beijing 100190, China;* orcid.org/0000-0002-8587-7818
Yu Chen − *Institute of High Energy Physics, Chinese Academy of Sciences, Beijing 100049, China*
Jiaou Wang − *Institute of High Energy Physics, Chinese Academy of Sciences, Beijing 100049, China*
Jing Zhou − *School of Materials Science and Engineering, Wuhan University of Technology, Wuhan 430070, China;* orcid.org/0000-0003-1774-085X
Yi Wang − *Key Laboratory of Material Modification by Laser, Ion and Electron Beams, Dalian University of Technology, Dalian 116024, China;* orcid.org/0000-0002-1747-0899
Qiliang Li − *Department of Advanced Manufacturing and Robotics, College of Engineering, Peking University, Beijing 100871, China*

Complete contact information is available at: https://pubs.acs.org/10.1021/jacs.5c01840

Author Contributions

[▽]H.W., X.L., and J.M. contributed equally to this work.

Notes

The authors declare no competing financial interest.

■ ACKNOWLEDGMENTS

This research is supported by the National Natural Science Foundation of China (T2495211), the National Key R&D Program of China (2020YFA0406202), the National Natural Science Foundation of China (Nos. 12274022, 11974042, 12374132, 12074052, 12261131506), FRF-EYIT-23-03, PHRD Fund (2147001149), and Beijing National Laboratory for Condensed Matter Physics (ZBJ2209270020). The authors gratefully acknowledge the cooperation of the beamline scientists at BSRF-1W1A and BSRF-4B9B beamlines and Ion Beam Material Laboratory (IBML) Peking University.

■ REFERENCES

(1) Chai, Y.; Liang, Y.; Xiao, C.; Wang, Y.; Li, B.; Jiang, D.; Pal, P.; Tang, Y.; Chen, H.; Zhang, Y.; Bai, H.; Xu, T.; Jiang, W.; Skowronski, W.; Zhang, Q.; Gu, L.; Ma, J.; Yu, P.; Tang, J.; Lin, Y.-H.; Yi, D.; Ralph, D. C.; Eom, C.-B.; Wu, H.; Nan, T. Voltage Control of Multiferroic Magnon Torque for Reconfigurable Logic-in-Memory. *Nat. Commun.* **2024**, *15* (1), 5975.
(2) Spaldin, N. A.; Ramesh, R. Advances in Magnetoelectric Multiferroics. *Nat. Mater.* **2019**, *18* (3), 203−212.
(3) Fiebig, M.; Lottermoser, T.; Meier, D.; Trassin, M. The Evolution of Multiferroics. *Nat. Rev. Mater.* **2016**, *1* (8), 16046.
(4) Wang, J.; Neaton, J. B.; Zheng, H.; Nagarajan, V.; Ogale, S. B.; Liu, B.; Viehland, D.; Vaithyanathan, V.; Schlom, D. G.; Waghmare, U. V.; Spaldin, N. A.; Rabe, K. M.; Wuttig, M.; Ramesh, R. Epitaxial $BiFeO_3$ Multiferroic Thin Film Heterostructures. *Science* **2003**, *299* (5613), 1719−1722.
(5) Hill, N. A. Why Are There so Few Magnetic Ferroelectrics? *J. Phys. Chem. B* **2000**, *104* (29), 6694−6709.
(6) Zhai, K.; Shang, D.-S.; Chai, Y.-S.; Li, G.; Cai, J.-W.; Shen, B.-G.; Sun, Y. Room-Temperature Nonvolatile Memory Based on a Single-Phase Multiferroic Hexaferrite. *Adv. Funct. Mater.* **2018**, *28* (9), 1705771.
(7) Li, Y.; Wang, Z.; Yao, J.; Yang, T.; Wang, Z.; Hu, J.-M.; Chen, C.; Sun, R.; Tian, Z.; Li, J.; Chen, L.-Q.; Viehland, D. Magnetoelectric Quasi-(0−3) Nanocomposite Heterostructures. *Nat. Commun.* **2015**, *6* (1), 6680.
(8) Amrillah, T.; Bitla, Y.; Shin, K.; Yang, T.; Hsieh, Y.-H.; Chiou, Y.-Y.; Liu, H.-J.; Do, T. H.; Su, D.; Chen, Y.-C.; Jen, S.-U.; Chen, L.-Q.; Kim, K. H.; Juang, J.-Y.; Chu, Y.-H. Flexible Multiferroic Bulk Heterojunction with Giant Magnetoelectric Coupling via van Der Waals Epitaxy. *ACS Nano* **2017**, *11* (6), 6122−6130.
(9) Tian, G.; Zhang, F.; Yao, J.; Fan, H.; Li, P.; Li, Z.; Song, X.; Zhang, X.; Qin, M.; Zeng, M.; Zhang, Z.; Yao, J.; Gao, X.; Liu, J. Magnetoelectric Coupling in Well-Ordered Epitaxial $BiFeO_3$/$CoFe_2O_4$/$SrRuO_3$ Heterostructured Nanodot Array. *ACS Nano* **2016**, *10* (1), 1025−1032.
(10) Baltz, V.; Manchon, A.; Tsoi, M.; Moriyama, T.; Ono, T.; Tserkovnyak, Y. Antiferromagnetic Spintronics. *Rev. Mod. Phys.* **2018**, *90* (1), 015005.
(11) Zhang, J.; Ma, J. C. Electric-Field Control of Magnetization Reversal at Room Temperature in $SmFeO_3$ Single-Phase Multiferroic Thin Film. *J. Alloys Compd.* **2023**, *934* (10), 167935.
(12) Gradauskaite, E.; Hunnestad, K. A.; Meier, Q. N.; Meier, D.; Trassin, M. Ferroelectric Domain Engineering Using Structural Defect Ordering. *Chem. Mater.* **2022**, *34* (14), 6468−6475.
(13) Lee, C.-H.; Orloff, N. D.; Birol, T.; Zhu, Y.; Goian, V.; Rocas, E.; Haislmaier, R.; Vlahos, E.; Mundy, J. A.; Kourkoutis, L. F.; Nie, Y.; Biegalski, M. D.; Zhang, J.; Bernhagen, M.; Benedek, N. A.; Kim, Y.; Brock, J. D.; Uecker, R.; Xi, X. X.; Gopalan, V.; Nuzhnyy, D.; Kamba, S.; Muller, D. A.; Takeuchi, I.; Booth, J. C.; Fennie, C. J.; Schlom, D. G. Exploiting Dimensionality and Defect Mitigation to Create Tunable Microwave Dielectrics. *Nature* **2013**, *502* (7472), 532−536.
(14) Fawcett, I. D.; Sunstrom, J. E.; Greenblatt, M.; Croft, M.; Ramanujachary, K. V. Structure, Magnetism, and Properties of Ruddlesden−Popper Calcium Manganates Prepared from Citrate Gels. *Chem. Mater.* **1998**, *10* (11), 3643−3651.
(15) Colfer, L.; Bagues, N.; Noor-A-Alam, M.; Schmidt, M.; Nolan, M.; McComb, D. W.; Keeney, L. Tilting and Distortion in the Multiferroic Aurivillius Phase $Bi_6Ti_3Fe_{1.5}Mn_{0.5}O_{18}$. *Chem. Mater.* **2024**, *36* (11), 5474−5486.
(16) Yun, Y.; Zhai, X.; Ma, C.; Huang, H.; Meng, D.; Cui, Z.; Wang, J.; Fu, Z.; Peng, R.; Brown, G. J.; Lu, Y. Growth of Single-Crystalline $Bi_6FeCoTi_3O_{18}$ Thin Films and Their Magnetic−Ferroelectric Properties. *Appl. Phys. Express* **2015**, *8* (5), 054001.
(17) Faraz, A.; Maity, T.; Schmidt, M.; Deepak, N.; Roy, S.; Pemble, M. E.; Whatmore, R. W.; Keeney, L. Direct Visualization of Magnetic-field-induced Magnetoelectric Switching in Multiferroic Aurivillius Phase Thin Films. *J. Am. Ceram. Soc.* **2017**, *100* (3), 975−987.
(18) Keeney, L.; Maity, T.; Schmidt, M.; Amann, A.; Deepak, N.; Petkov, N.; Roy, S.; Pemble, M. E.; Whatmore, R. W. Magnetic Field-Induced Ferroelectric Switching in Multiferroic Aurivillius Phase Thin Films at Room Temperature. *J. Am. Ceram. Soc.* **2013**, *96* (8), 2339−2357.
(19) Pitcher, M. J.; Mandal, P.; Dyer, M. S.; Alaria, J.; Borisov, P.; Niu, H.; Claridge, J. B.; Rosseinsky, M. J. Tilt Engineering of Spontaneous Polarization and Magnetization above 300 K in a Bulk Layered Perovskite. *Science* **2015**, *347* (6220), 420−424.
(20) Moore, K.; O'Connell, E. N.; Griffin, S. M.; Downing, C.; Colfer, L.; Schmidt, M.; Nicolosi, V.; Bangert, U.; Keeney, L.; Conroy, M. Charged Domain Wall and Polar Vortex Topologies in a Room-Temperature Magnetoelectric Multiferroic Thin Film. *ACS Appl. Mater. Interfaces* **2022**, *14* (4), 5525−5536.

(21) Luo, L.; Sun, L.; Long, Y.; Wang, X.; Li, Q.; Liang, K.; Zhao, J.; Yan, W.; Sun, Q.; Su, J.; Lu, X.; Zhu, J. Multiferroic Properties of Aurivillius Structure $Bi_4SmFeTi_3O_{15}$ Thin Films. *J. Mater. Sci.: Mater. Electron.* **2019**, *30* (10), 9945−9954.
(22) Venkata Ramana, E.; Prasad, N. V.; Figueiras, F.; Lajaunie, L.; Arenal, R.; Otero-Irurueta, G.; Valente, M. A. The Growth and Improved Magnetoelectric Response of Strain-Modified Aurivillius $SrBi_{4.25}La_{0.75}Ti_4FeO_{18}$ Thin Films. *Dalton Trans.* **2019**, *48* (35), 13224−13241.
(23) Su, J.; Long, Y.; Li, Q.; Lu, C.; Liang, K.; Li, J.; Luo, L.; Sun, L.; Lu, X.; Zhu, J. Room-Temperature Magnetoelectric Coupling in $Bi_4LaFeTi_3O_{15}$ Multiferroic Films. *J. Alloys Compd.* **2018**, *747* (30), 1002−1007.
(24) Wang, M.; Tan, G. Multiferroic Properties of $Pb_2Fe_2O_5$ Ceramics. *Mater. Res. Bull.* **2011**, *46* (3), 438−441.
(25) Beklešovas, B.; Stankus, V.; Link, J.; Stern, R. Structural, Ferroelectric and Magnetic Properties of Lead Ferrite ($Pb_2Fe_2O_5$) Thin Films Synthesized by Reactive Magnetron Deposition. *Thin Solid Films* **2020**, *708* (31), 138124.
(26) Batuk, D.; Hadermann, J.; Abakumov, A.; Vranken, T.; Hardy, A.; Van Bael, M.; Van Tendeloo, G. Layered Perovskite-Like $Pb_2Fe_2O_5$ Structure as a Parent Matrix for the Nucleation and Growth of Crystallographic Shear Planes. *Inorg. Chem.* **2011**, *50* (11), 4978−4986.
(27) Stone, G.; Ophus, C.; Birol, T.; Ciston, J.; Lee, C.-H.; Wang, K.; Fennie, C. J.; Schlom, D. G.; Alem, N.; Gopalan, V. Atomic Scale Imaging of Competing Polar States in a Ruddlesden−Popper Layered Oxide. *Nat. Commun.* **2016**, *7* (1), 167935.
(28) Martin, S.; Baboux, N.; Albertini, D.; Gautier, B. A New Technique Based on Current Measurement for Nanoscale Ferroelectricity Assessment: Nano-Positive up Negative Down. *Rev. Sci. Instrum.* **2017**, *88* (2), 023901.
(29) Fukunaga, M.; Noda, Y. New Technique for Measuring Ferroelectric and Antiferroelectric Hysteresis Loops. *J. Phys. Soc. Jpn.* **2008**, *77* (6), 064706.
(30) Zhang, J. X.; He, Q.; Trassin, M.; Luo, W.; Yi, D.; Rossell, M. D.; Yu, P.; You, L.; Wang, C. H.; Kuo, C. Y.; Heron, J. T.; Hu, Z.; Zeches, R. J.; Lin, H. J.; Tanaka, A.; Chen, C. T.; Tjeng, L. H.; Chu, Y.-H.; Ramesh, R. Microscopic Origin of the Giant Ferroelectric Polarization in Tetragonal-like $BiFeO_3$. *Phys. Rev. Lett.* **2011**, *107* (14), 147602.
(31) Li, H.; Yang, Y.; Deng, S.; Zhang, L.; Cheng, S.; Guo, E.-J.; Zhu, T.; Wang, H.; Wang, J.; Wu, M.; Gao, P.; Xiang, H.; Xing, X.; Chen, J. Role of Oxygen Vacancies in Colossal Polarization in $SmFeO_{3-\delta}$ Thin Films. *Sci. Adv.* **2022**, *8* (13), No. eabm8550.
(32) Liu, Y.; Tan, G.; Guo, M.; Chai, Z.; Lv, L.; Xue, M.; Ren, X.; Li, J.; Ren, H.; Xia, A. Multiferroic Properties of La/Er/Mn/Co Multi-Doped $BiFeO_3$ Thin Films. *Ceram. Int.* **2019**, *45* (9), 11765−11775.
(33) Liu, J.; Ren, J.-C.; Shen, T.; Liu, X.; Butch, C. J.; Li, S.; Liu, W. Asymmetric Schottky Contacts in van Der Waals Metal-Semiconductor-Metal Structures Based on Two-Dimensional Janus Materials. *Research* **2020**, *2020*, 1−8.
(34) Mion, T.; Staruch, M.; Bussmann, K.; Karapetrov, G.; van 't Erve, O.; Mills, S.; Ryou, H.; Goswami, R.; Callahan, P. G.; Rowenhorst, D. J.; Qadri, S. B.; Lofland, S. E.; Finkel, P. Effect of Hf Alloying on Magnetic, Structural, and Magnetostrictive Properties in FeCo Films for Magnetoelectric Heterostructure Devices. *APL Mater.* **2023**, *11* (11), 111107.
(35) Kumar, M.; Shankar, S.; Kumar, A.; Anshul, A.; Jayasimhadri, M.; Thakur, O. P. Progress in Multiferroic and Magnetoelectric Materials: Applications, Opportunities and Challenges. *J. Mater. Sci.: Mater. Electron.* **2020**, *31* (22), 19487−19510.
(36) Kim, M.; Kim, D.; Aktas, B.; Choi, H.; Puigmartí-Luis, J.; Nelson, B. J.; Pané, S.; Chen, X. Strain-Sensitive Flexible Magnetoelectric Ceramic Nanocomposites. *Adv. Mater. Technol.* **2023**, *8* (6), 2202097.
(37) Xie, S.; Ma, F.; Liu, Y.; Li, J. Multiferroic $CoFe_2O_4$−$Pb(Zr_{0.52}Ti_{0.48})O_3$ Core-Shell Nanofibers and Their Magnetoelectric Coupling. *Nanoscale* **2011**, *3* (8), 3152.
(38) Gupta, R.; Chaudhary, S.; Kotnala, R. K. Interfacial Charge Induced Magnetoelectric Coupling at $BiFeO_3/BaTiO_3$ Bilayer Interface. *ACS Appl. Mater. Interfaces* **2015**, *7* (16), 8472−8479.
(39) Chu, Z.; Shi, H.; Shi, W.; Liu, G.; Wu, J.; Yang, J.; Dong, S. Enhanced Resonance Magnetoelectric Coupling in (1−1) Connectivity Composites. *Adv. Mater.* **2017**, *29* (19), 1606022.
(40) Gupta, R.; Kotnala, R. K. A Review on Current Status and Mechanisms of Room-Temperature Magnetoelectric Coupling in Multiferroics for Device Applications. *J. Mater. Sci.* **2022**, *57* (27), 12710−12737.
(41) Chen, X.-Z.; Hoop, M.; Shamsudhin, N.; Huang, T.; Özkale, B.; Li, Q.; Siringil, E.; Mushtaq, F.; Di Tizio, L.; Nelson, B. J.; Pané, S. Hybrid Magnetoelectric Nanowires for Nanorobotic Applications: Fabrication, Magnetoelectric Coupling, and Magnetically Assisted In Vitro Targeted Drug Delivery. *Adv. Mater.* **2017**, *29* (8), 1605458.
(42) Zhang, Y.; Wu, X.; Ding, J.; Su, B.; Chen, Z.; Xiao, Z.; Wu, C.; Wei, D.; Sun, J.; Luo, F.; Yin, H.; Fan, H. Wireless-Powering Deep Brain Stimulation Platform Based on 1D-Structured Magnetoelectric Nanochains Applied in Antiepilepsy Treatment. *ACS Nano* **2023**, *17* (16), 15796−15809.
(43) Song, H.; Kim, D.; Abbasi, S. A.; Latifi Gharamaleki, N.; Kim, E.; Jin, C.; Kim, S.; Hwang, J.; Kim, J.-Y.; Chen, X.-Z.; Nelson, B. J.; Pané, S.; Choi, H. Multi-Target Cell Therapy Using a Magnetoelectric Microscale Biorobot for Targeted Delivery and Selective Differentiation of SH-SY5Y Cells *via* Magnetically Driven Cell Stamping. *Mater. Horiz.* **2022**, *9* (12), 3031−3038.
(44) Kim, D.; Efe, I.; Torlakcik, H.; Terzopoulou, A.; Veciana, A.; Siringil, E.; Mushtaq, F.; Franco, C.; von Arx, D.; Sevim, S.; Puigmartí-Luis, J.; Nelson, B.; Spaldin, N. A.; Gattinoni, C.; Chen, X.-Z.; Pané, S. Magnetoelectric Effect in Hydrogen Harvesting: Magnetic Field as a Trigger of Catalytic Reactions. *Adv. Mater.* **2022**, *34* (19), 2110612.
(45) Long, J.; Ivanov, M. S.; Khomchenko, V. A.; Mamontova, E.; Thibaud, J.-M.; Rouquette, J.; Beaudhuin, M.; Granier, D.; Ferreira, R. A. S.; Carlos, L. D.; Donnadieu, B.; Henriques, M. S. C.; Paixão, J. A.; Guari, Y.; Larionova, J. Room Temperature Magnetoelectric Coupling in a Molecular Ferroelectric Ytterbium(III) Complex. *Science* **2020**, *367* (6478), 671−676.
(46) Mushtaq, F.; Chen, X.; Torlakcik, H.; Steuer, C.; Hoop, M.; Siringil, E. C.; Marti, X.; Limburg, G.; Stipp, P.; Nelson, B. J.; Pané, S. Magnetoelectrically Driven Catalytic Degradation of Organics. *Adv. Mater.* **2019**, *31* (28), 1901378.
(47) Chen, A.; Dai, Y.; Eshghinejad, A.; Liu, Z.; Wang, Z.; Bowlan, J.; Knall, E.; Civale, L.; MacManus-Driscoll, J. L.; Taylor, A. J.; Prasankumar, R. P.; Lookman, T.; Li, J.; Yarotski, D.; Jia, Q. Competing Interface and Bulk Effect−Driven Magnetoelectric Coupling in Vertically Aligned Nanocomposites. *Adv. Sci.* **2019**, *6* (19), 1901000.
(48) Meng, D.; Zhai, X.; Ma, C.; Huang, H.; Yun, Y.; Huang, Y.; Fu, Z.; Peng, R.; Mao, X.; Chen, X.; Brown, G.; Lu, Y. Self-Modulated Nanostructures in Super-Large-Period $Bi_{11}(Fe_5CoTi_3)_{10/9}O_{33}$ Epitaxial Thin Films. *Appl. Phys. Lett.* **2015**, *106* (21), 212906.
(49) Campanini, M.; Trassin, M.; Ederer, C.; Erni, R.; Rossell, M. D. Buried In-Plane Ferroelectric Domains in Fe-Doped Single-Crystalline Aurivillius Thin Films. *ACS Appl. Electron. Mater.* **2019**, *1* (6), 1019−1028.
(50) Gradauskaite, E.; Meier, Q. N.; Gray, N.; Sarott, M. F.; Scharsach, T.; Campanini, M.; Moran, T.; Vogel, A.; Del Cid-Ledezma, K.; Huey, B. D.; Rossell, M. D.; Fiebig, M.; Trassin, M. Defeating Depolarizing Fields with Artificial Flux Closure in Ultrathin Ferroelectrics. *Nat. Mater.* **2023**, *22* (12), 1492−1498.
(51) Li, T.; Deng, S.; Liu, H.; Sun, S.; Li, H.; Hu, S.; Liu, S.; Xing, X.; Chen, J. Strong Room-Temperature Ferroelectricity in Strained $SrTiO_3$ Homoepitaxial Film. *Adv. Mater.* **2021**, *33* (21), 2008316.
(52) Li, S.; Wang, J.; Zhang, Q.; Roldan, M. A.; Shan, L.; Jin, Q.; Chen, S.; Wu, Z.; Wang, C.; Ge, C.; He, M.; Guo, H.; Gu, L.; Jin, K.; Guo, E.-J. Maximization of Ferromagnetism in $LaCoO_3$ Films by Competing Symmetry. *Phys. Rev. Mater.* **2019**, *3* (11), 114409.

https://doi.org/10.1021/jacs.5c01840
J. Am. Chem. Soc. 2025, 147, 24382−24391

(53) Zhang, L.; Chen, J.; Fan, L.; Diéguez, O.; Cao, J.; Pan, Z.; Wang, Y.; Wang, J.; Kim, M.; Deng, S.; Wang, J.; Wang, H.; Deng, J.; Yu, R.; Scott, J. F.; Xing, X. Giant Polarization in Super-Tetragonal Thin Films through Interphase Strain. *Science* **2018**, *361* (6401), 494−497.
(54) Ning, S.; Kumar, A.; Klyukin, K.; Cho, E.; Kim, J. H.; Su, T.; Kim, H.-S.; LeBeau, J. M.; Yildiz, B.; Ross, C. A. An Antisite Defect Mechanism for Room Temperature Ferroelectricity in Orthoferrites. *Nat. Commun.* **2021**, *12* (1), 4298.
(55) Cohen, R. E. Origin of Ferroelectricity in Perovskite Oxides. *Nature* **1992**, *358* (6382), 136−138.
(56) Blöchl, P. E. Projector Augmented-Wave Method. *Phys. Rev. B* **1994**, *50* (24), 17953−17979.
(57) Kresse, G.; Furthmüller, J. Efficient Iterative Schemes for *Ab Initio* Total-Energy Calculations Using a Plane-Wave Basis Set. *Phys. Rev. B* **1996**, *54* (16), 11169−11186.
(58) Kresse, G.; Furthmüller, J. Efficiency of Ab-Initio Total Energy Calculations for Metals and Semiconductors Using a Plane-Wave Basis Set. *Comput. Mater. Sci.* **1996**, *6* (1), 15−50.
(59) Delley, B. An All-electron Numerical Method for Solving the Local Density Functional for Polyatomic Molecules. *J. Chem. Phys.* **1990**, *92* (1), 508−517.
(60) Perdew, J. P.; Burke, K.; Ernzerhof, M. Generalized Gradient Approximation Made Simple. *Phys. Rev. Lett.* **1996**, *77* (18), 3865−3868.
(61) MacLaren, I.; Wang, L. Q.; Schaffer, B.; Ramasse, Q. M.; Craven, A. J.; Selbach, S. M.; Spaldin, N. A.; Miao, S.; Kalantari, K.; Reaney, I. M. Novel Nanorod Precipitate Formation in Neodymium and Titanium Codoped Bismuth Ferrite. *Adv. Funct. Mater.* **2013**, *23* (6), 683−689.
(62) Fong, D. D.; Cionca, C.; Yacoby, Y.; Stephenson, G. B.; Eastman, J. A.; Fuoss, P. H.; Streiffer, S. K.; Thompson, C.; Clarke, R.; Pindak, R.; Stern, E. A. Direct Structural Determination in Ultrathin Ferroelectric Films by Analysis of Synchrotron X-Ray Scattering Measurements. *Phys. Rev. B* **2005**, *71* (14), 144112.
(63) Yang, Y.; Dansou, C.; Paillard, C.; He, J.; Xiang, H.; Bellaiche, L. Large Photostriction near the Phase Boundary in $BiFeO_3$ under Varying Epitaxial Strain. *Phys. Rev. B* **2024**, *109* (18), 184111.

https://doi.org/10.1021/jacs.5c01840
J. Am. Chem. Soc. 2025, 147, 24382−24391